ACS APPLIED MATERIALS & INTERFACES

Research Article

www.acsami.org

Atomic-Oxygen-Durable and Electrically-Conductive CNT-POSS-Polyimide Flexible Films for Space Applications

Nurit Atar,*[,†,‡] Eitan Grossman,[†] Irina Gouzman,[†] Asaf Bolker,[†] Vanessa J. Murray,[§] Brooks C. Marshall,[§] Min Qian,[§] Timothy K. Minton,[§] and Yael Hanein[‡,∥]

[†]Space Environment Department, Soreq NRC, Yavne 81800, Israel

[‡]School of Electrical Engineering and [∥]Tel Aviv University Center for Nanoscience and Nanotechnology, Tel-Aviv University, Ramat Aviv, Tel-Aviv 69978, Israel

[§]Department of Chemistry and Biochemistry, Montana State University, Bozeman, Montana 59717, United States

ABSTRACT: In low Earth orbit (LEO), hazards such as atomic oxygen (AO) or electrostatic discharge (ESD) degrade polymeric materials, specifically, the extensively used polyimide (PI) Kapton. We prepared PI-based nanocomposite films that show both AO durability and ESD protection by incorporating polyhedral oligomeric silsesquioxane (POSS) and carbon nanotube (CNT) additives. The unique methods that are reported prevent CNT agglomeration and degradation of the CNT properties that are common in dispersion-based processes. The influence of the POSS content on the electrical, mechanical, and thermo-optical properties of the CNT−POSS−PI films was investigated and compared to those of control PI and CNT−PI films. CNT−POSS−PI films with 5 and 15 wt % POSS content exhibited sheet resistivities as low as 200 Ω/□, and these resistivities remained essentially unchanged after exposure to AO with a fluence of ∼2.3 × 10^{20} O atoms cm^{-2}. CNT−POSS−PI films with 15 wt % POSS content exhibited an erosion yield of 4.8 × 10^{-25} cm^3 O $atom^{-1}$ under 2.3 × 10^{20} O atoms cm^{-2} AO fluence, roughly one order of magnitude lower than that of pure PI films. The durability of the conductivity of the composite films was demonstrated by rolling film samples with a tight radius up to 300 times. The stability of the films to thermal cycling and ionizing radiation was also demonstrated. These properties make the prepared CNT−POSS−PI films with 15 wt % POSS content excellent candidates for applications where AO durability and electrical conductivity are required for flexible and thermally stable materials. Hence, they are suggested here for LEO applications such as the outer layers of spacecraft thermal blankets.

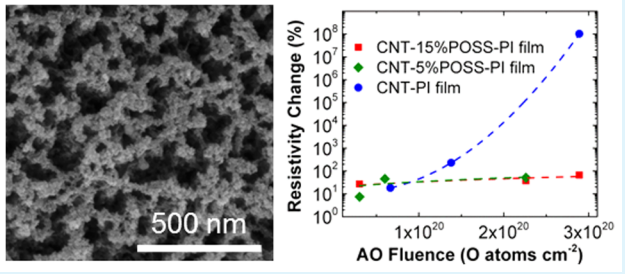

KEYWORDS: *CNT sheets, polyimide, POSS, nanocomposites, electrical conductivity, LEO space environment, atomic oxygen*

1. INTRODUCTION

The low Earth orbit (LEO) environment is characterized by hazards such as atomic oxygen (AO), plasma, UV radiation, ionizing radiation, ultrahigh vacuum, thermal cycling, micrometeoroids, and orbital debris.[1] Polyimide (PI) is commonly used as an external layer in a multilayer structure of thermal blankets to insulate satellites from solar radiation.[2] Despite their excellent radiation and chemical resistance as well as their thermal stability,[3] PI films erode significantly under AO exposure. The resistance of polymer films to AO attack can be improved by applying AO-durable oxide-based coatings such as aluminum oxide, silicon dioxide, tin oxide, or indium tin oxide (ITO).[4−7] However, these inorganic coatings are prone to crack, and they cannot tolerate folding or bending with small radii.[4] In addition, coatings may become compromised by micrometeoroid or debris impacts in LEO. An opening in a coating allows AO to attack the substrate and undercut the coating, thereby creating an ever-growing region of erosion. Introducing fluoropolymers to the inorganic coatings was found to improve the strain-to-failure of the protective coatings.[8] Ion implantation of metals or semiconductors into the polymer surfaces can also produce an effective AO-resistant layer that maintains some flexibility.[9−11]

Another approach to mitigate AO-induced degradation of PI films is to incorporate oxidation-resistant components in the form of chemical functional groups or additives.[12−15] Bulk AO durability may be enhanced through the incorporation of polyhedral oligomeric silsesquioxane (POSS) monomers either through copolymerization or blending.[16−20] POSS monomers are organic/inorganic molecules based on a silicon/oxygen cage with stoichiometry, Si_2O_3. Under AO exposure, the POSS cage oxidizes further to SiO_2 and creates a self-passivating network on the surface of POSS-containing films.[17] Although such films have improved AO resistance, they are electrically insulating. Thus, when they are exposed to space plasma they are likely to

Received: March 12, 2015
Accepted: May 6, 2015
Published: May 6, 2015

DOI: 10.1021/acsami.5b02200
ACS Appl. Mater. Interfaces 2015, 7, 12047−12056

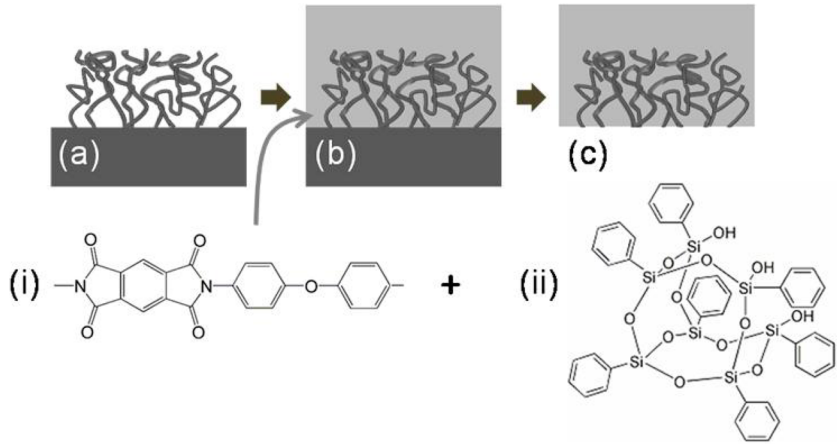

Figure 1. Schematic illustration of CNT−POSS−PI film fabrication process. (a) A ∼9 μm thick CNT sheet is first grown by CVD on a prepatterned Si substrate. (b) A POSS−PAA blend, composed of (i) PMDA−ODA monomer and (ii) trisilanolphenyl-POSS, is then infiltrated into the CNT sheet. (c) The free-standing CNT−POSS−PI film is mechanically peeled from the substrate after curing.

become charged, making them subject to electrostatic discharge (ESD) and creating a hazard for spacecraft electronics.

To avoid ESD problems associated with PI films, electrically conductive PI-based films can be produced by incorporating electrically conductive additives, such as carbon nanotubes (CNTs).[21−28] We recently developed conductive CNT−PI composite films using infiltration of polyamic acid precursor into entangled CNT sheets with cup-stacked nanostructure that were grown by chemical vapor deposition (CVD).[29] After curing, the PI matrix imparted mechanical stability, robustness, and flexibility to the composite film, while the porous CNT structure provided electrical conductivity. The resulting CNT−PI films have demonstrated high isotropic electrical conductivity and compatibility with the geo-synchronous Earth orbit (GEO) environment. However, such CNT−PI composites are expected to erode under AO exposure, which is the dominant species at LEO altitudes. Hence, in the current research, POSS−PI, rather than pure PI, was infiltrated into as-grown entangled CVD-grown CNT sheets, thus improving the flexibility and mechanical stability of the CVD-grown CNT sheets and enhancing the resistance to AO attack. The CNTs were used in their as-grown sheet configuration, and treatments to improve wettability or homogeneity, commonly applied in CNT powder dispersions, were thus avoided.[30]

Electrically conductive and flexible CNT−POSS−PI films were produced, and a systematic investigation was conducted to identify the effect of the POSS content on the electrical, mechanical, and thermo-optical properties of the obtained films. In addition, the durability of the CNT−POSS−PI films to simulated LEO environmental effects—thermal cycling, ionizing radiation, and AO exposure was studied as well.

2. EXPERIMENTAL METHODS

2.1. Materials. Entangled CNT sheets were grown by the CVD technique on Si wafers with a 500 nm thermal oxide layer (SiO_2).[31] Substrates were coated with a catalytic layer of Ni with a thickness of 2.5 nm by means of an electron beam evaporator. The CVD procedure included the gradual increase of the furnace temperature to 900 °C within 20 min and a growth duration of 5 min under hydrogen and ethylene flows of 1000 and 20 sccm, respectively. The resulting CNT sheets were characterized and found to have an average sheet thickness of 9 ± 2 μm, a CNT content of 14 vol %, and cup-stacked CNT (CSCNT) nanostructure.[29] PI matrices with different POSS content (0, 5, and 15 wt %) were prepared. A polyamic acid (PAA) solution of 15 wt % pyromellitic dianhydryde−oxydianiline (PMDA−ODA) in *N*-methyl-2-pyrrolidone (NMP) was purchased from Sigma-Aldrich (575801) to form the pure PI matrix (0 wt % POSS). Nanoreinforced POSS-polyimide PAA blends (15 wt %) in NMP with trisilanolphenyl (TSP)-POSS content of 5 and 15 wt % were purchased from Hybrid Plastics (PM1215.5 and PM1215.15, respectively) to form the POSS−PI matrices. The PAA blends were further diluted by NMP (Sigma-Aldrich, 443778) with a ratio of 1:3 (PAA:NMP).

2.2. Nanocomposite Film Preparation. POSS−PI blends with varying POSS content (0, 5, and 15 wt %) were infiltrated into the as-grown CSCNT sheets as shown schematically in Figure 1. Following the solution casting, penetration between the CNTs was achieved, and the CNT−POSS−PAA systems were then cured. The POSS−PAA solution was cured into a POSS−PI supporting matrix by gradual heating to 350 °C in a nitrogen atmosphere, according to a process developed by DuPont, Inc.[18,32] During heating, thermal imidization occurred, followed by ring-closure and loss of water.[33]

To facilitate the polymer infiltration, a low-viscosity POSS−PAA blend in NMP (POSS−PAA/NMP, 1:3) was used. The dilution also improved the thickness control and the homogeneity of the resulting films. CNT sheets with an area of up to 55 cm^2 were cast by the diluted PAA with a pouring ratio of 67 $\mu L\ cm^{-2}$. The total thickness of the CNT−POSS−PI films after curing was 15 ± 2 μm with only the bottom 9 ± 2 μm layer containing CNTs. The polymeric layer on top was intended to improve the mechanical robustness of the composite film. This technique is also usable for large film formation depending on the CVD reactor size; for example, in the current study, films were prepared with surface area of up to 55 cm^2.

Free-standing flexible CNT−POSS−PI films (Figure 1c) were obtained by peeling the nanocomposites from the substrates. The removal of the nanocomposite from the substrate was facilitated by the low adhesion between the CNTs and the oxide layer on the Si wafer.

2.3. Morphological Observation. The morphologies of the cross-section facets and bottom surfaces of the samples were characterized with the use of a high-resolution scanning electron microscope (HRSEM), Magellan model from FEI Co.

2.4. Mechanical Characterization. Tensile tests were performed with the use of dynamic mechanical analysis (DMA)—Q800 from TA Instruments—and the data were analyzed by the Universal Analysis 2000 software, version 4.5A. Stress versus strain curves were recorded at room temperature. The procedure included control over the applied force with a rate of 3.00 N min^{-1}. The samples were cut into rectangular shapes of 11.10 mm × 5.01 mm. The maximum stress that the films could withstand before failing was reported as the ultimate tensile stress (UTS). The Young's modulus was calculated as the slope of the stress-versus-strain curve in the linear range.

2.5. Electrical Characterization. The electrical properties of the samples in the lateral direction were measured with the use of a source

DOI: 10.1021/acsami.5b02200
ACS Appl. Mater. Interfaces 2015, 7, 12047−12056

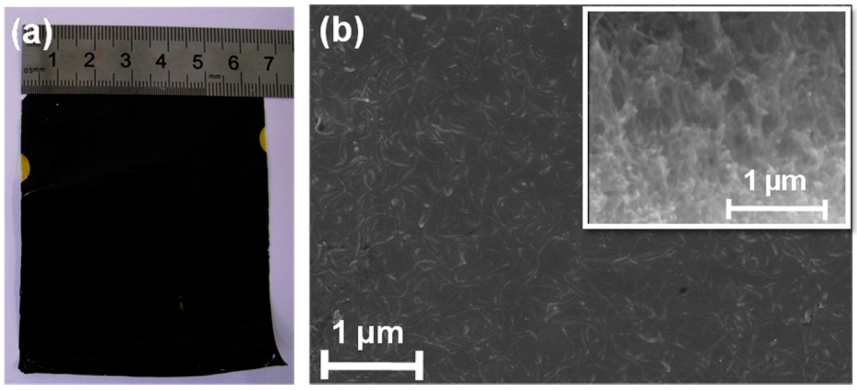

Figure 2. (a) Photograph of CNT−PI film with area of ∼55 cm^2. (b) HRSEM images of the CNT−PI film's surface and its cross-section (inset).

meter (Keithley 2400, Keithley Instruments). The electrical properties of the CNT sheets were measured by attaching the source meter probes to parallel silver paint (5001-AB, SPI Supplies) electrodes that were applied to the surfaces of the samples. The CNT-based nanocomposite films were tested with a nondestructive configuration, where the electrodes were pressed on the samples' bottom surfaces using a weight, which prevented irreversibly marking the sample.

A direct current was supplied to the sample, and the built-up voltage was measured in the lateral direction for both current-versus-voltage and resistivity measurements. The current-versus-voltage curves were obtained for an area of 0.5 cm × 1 cm, which was defined by two parallel electrodes. To perform sheet resistivity measurements, a set of parallel electrodes was applied across a sample surface with dimensions of 0.5 cm × 4 cm to form several square segments, each with an area of ∼25 mm^2. The lateral resistance of the samples, R, was measured for different areas with a constant width (5 mm) w, and increasing lengths L (up to 4 cm). The sheet resistivity ρ_s, in units of Ω/□, is related to the lateral resitance according to the relation

$$R = \rho_s \frac{L}{w} + R_c \tag{1}$$

where R_c is the contact resistance. A linear trend line was fitted to the lateral resistance R versus the number of measured segments L/w. ρ_s was determined from the slope, and the contact resistance was expressed by its intercept with the y-axis. Thus, the sheet resistivities were extracted while eliminating the contribution of the contact resistance.

The sheet resistivity measurement was repeated after rolling to examine the durability of the electrical conductivity of the CNT−PI films under mechanical manipulation. The films were rolled manually up to 300 times around a ceramic rod of 2.9 mm diameter, and their resistivity was measured after every 50 cycles.

The temperature dependence of the sheet resistivity was measured by the van der Pauw four-point probe method that eliminates influence of the contact resistances and sample geometry.[34] The sample temperature was controlled in the range from −160 to 200 °C using a THMS600 Linkam stage working in a nitrogen atmosphere. Current was supplied to the sample using a Keithley 220 programmable current source and measured with a Keithley 485 picoammeter. Four silver contacts were applied by spreading silver paint dots on the corners of the bottom surfaces of the 5 mm × 5 mm samples. Each of the four contacts was connected to a very high input impedance (>200 TΩ) Keithley 6514 electrometer. The voltage difference between each of the two electrometers was measured using a Keithley 2000 multimeter. The current source, electrometers, multimeter, and sample contacts were connected to a Keithley 7001 switch. All elements in the system were controlled with a computer.

2.6. Response under Simulated Space Environmental Conditions. *2.6.1. Thermo-Optical Properties.* As radiation is the dominant mechanism for heat transfer in a vacuum environment, the equilibrium temperature, T (K), of an object in space is governed by the heat it absorbs from the sun, related to the solar absorptance α_s, and the heat it radiates to its surroundings according to its emittance ε. Subject to these constraints, the equilibrium temperature of the CNT-based composite films was calculated by[1]

$$T = \left(\frac{\alpha_s}{\varepsilon}\right)^{1/4} \left(\frac{SA_n}{\sigma A}\right)^{1/4} \tag{2}$$

where S (W m^{-2}) is the solar flux per unit area at the relevant orbit, A_n (m^2) is the film's surface area normal to the solar flux, A (m^2) is its total surface area, and σ (5.67×10^{-8} W m^{-2} K^{-4}) is the Stefan−Boltzmann constant. The calculation was related to samples with sphere geometry (normal area factor of $A_n/A = 0.25$)[35] and a solar flux of 1366.1 W m^{-2}, which is the average flux value at 1 AU from the sun.[36] The thermo-optical characteristics of the films, α_s and ε, were measured at room temperature by an IR/solar reflectometer (TESA 2000, AZ technologies) using an integrating sphere.

2.6.2. Thermal Cycling. The electrical conductivity of the CNT−POSS−PI films (5 mm × 5 mm) under thermal cycling was tested by the four-point van der Pauw technique, described above, while cycling the temperature of the samples from −100 to 140 °C.

2.6.3. Ionizing Radiation. The ionizing radiation in space was simulated by exposure to γ radiation.[37−40] The CNT-based nanocomposite films were exposed to a maximum γ radiation of 9.9 MGy by a ^{60}Co source, equivalent to ∼15 years in GEO or thousands of years in LEO.[41] A high dose rate of 0.1 MGy h^{-1} was obtained for a sample distance of 7 cm from the source, as measured by a perspex dosimeter from Harwell. The films were exposed to γ radiation for several dose increments, and the effect on their electrical resistivity was measured after each dose increment.

2.6.4. Atomic- Oxygen Exposure. Ground-based AO exposures of the composite films were performed using a laser detonation hyperthermal AO pulsed beam, operating at a repetition rate of 2 Hz.[42] The AO beam contained O atoms that were generated by the laser-induced breakdown of O_2 gas in a conical nozzle with the use of a 7 Joules per pulse CO_2 laser. The hyperthermal beam contains mainly neutral O atoms and O_2 molecules, with an ionic component of <0.01%. The mole fraction of atomic oxygen in the beam was above 70%. Kinetic energies of the fast O atoms in the beam averaged 5.2 eV, with a full width at half-maximum in the distribution of ∼1.5 eV. The films were cut into rectangles of 0.5 cm × 4 cm size and attached to Si substrates with aluminum tape, leaving their electrically conductive bottom surfaces (containing CNTs) exposed to the AO environment. The erosion yield of the films was calculated according to a standard test method, ASTM E2089, as follows:[43]

$$E = \frac{\Delta m}{A\rho F} \tag{3}$$

where E is the erosion yield (cm^3 O atom^{-1}), Δm represents the mass loss (g), A is the exposed area (cm^2), ρ denotes the sample's density (g cm^{-3}), and F is the O atom fluence (O atoms cm^{-2}), as determined from the erosion of a Kapton H reference sample.[42] The composites were exposed to a maximum fluence of 2.9×10^{20} O atoms cm^{-2},

DOI: 10.1021/acsami.5b02200
ACS Appl. Mater. Interfaces 2015, 7, 12047−12056

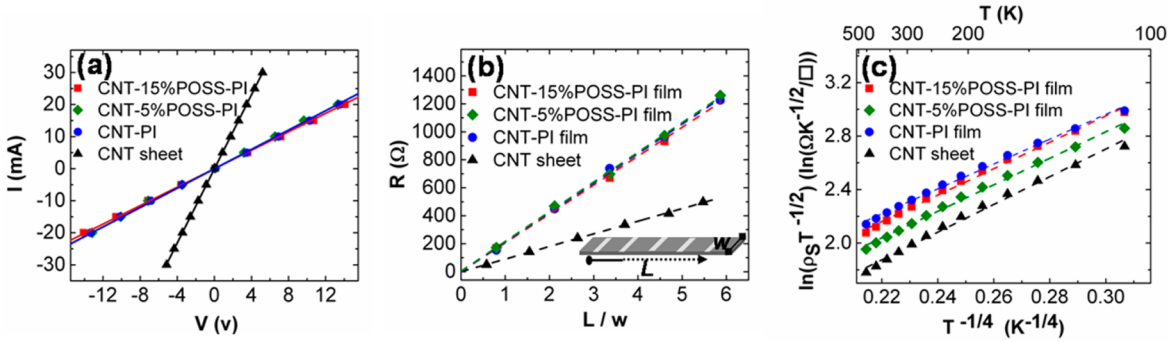

Figure 3. Electrical properties of CNT−POSS−PI films (0, 5, and 15 wt % POSS content) and pure CNT sheet in blue circles, green diamonds, red squares, and black triangles, respectively. (a) Current vs voltage curves along the lateral direction of the films. (b) Sheet resistance as a function of the number of measured squares (L/w). Each sheet resistivity was calculated as the slope of the corresponding linear trend line. (c) Temperature-dependent sheet resistivity.

equivalent to half a year at an altitude of 500 km.[44] Δm was measured by a microbalance, Sartorius SE2 (readability of ±0.1 μg) after reaching a steady state in terms of humidity absorption. The etch depth, Δd (cm), was evaluated by the measured Δm according to

$$\Delta d = \frac{\Delta V}{A} = \frac{\Delta m/\rho}{A} \quad (4)$$

where ΔV (cm^3) is the etched volume, which is calculated from Δm and ρ. In the case of constant erosion yield the expected Δd can be calculated by

$$\Delta d = E{\cdot}F \quad (5)$$

If the erosion yield is not constant, as in the case of the POSS-containing samples, the etch depth cannot be calculated so simply and requires knowledge of the functional dependence of the erosion yield on O atom fluence.

3. RESULTS AND DISCUSSION

3.1. Morphological Characterization. CNT composites were prepared by infiltration of PI-based blends into CNT sheets. A representative photograph of a resulting composite is displayed in Figure 2a. The top surface morphology of a typical CNT-based film was examined by HRSEM as seen in Figure 2b. A homogeneous distribution of CNTs in the PI matrix is clearly observed. This result indicates that the preparation procedure preserves the homogeneous structure of the entangled CNT sheet without agglomeration after PI infiltration. The CNTs observed on the surface of the film are part of the CNT network that expands throughout the 9 μm thickness of the CNT layer, as shown in the cross-sectional image in the inset of Figure 2b.

3.2. Electrical Characterization. Typical current-versus-voltage curves measured along the conductive bottom surfaces of the composite films are shown in Figure 3a, revealing the ohmic nature of the resistivity at room temperature. The macroscopic lateral resistances of the composite films and CNT sheets, R, were then measured for different areas with a constant width (w = 5 mm) and increasing lengths (L = 0.5 to 4 cm). Typical data (for one sample of each type) are plotted in Figure 3b, and throughout this manuscript, with blue circles, green diamonds, and red squares representing values for CNT−POSS−PI films with POSS contents of 0, 5, and 15 wt %, respectively, while values for the pure CNT sheet are represented by black triangles. The sheet resistivity ρ_s was calculated according to (1) as the slope of the linear trend line of the experimental data (R vs L/w). This measurement was repeated for several samples of each type, and the average sheet resistivities, which well satisfy the ESD criterion,[45] are presented in Table 1. The volume (bulk) resistivity of the CNT-containing layer in each composite film was derived by multiplying the average sheet resistivity (measured at the bottom surface) by the 9 μm thickness of the CNT conductive layer. The durability of the film to ESD is influenced only by the sheet resistivity of the CNT-containing surface of the film, which is intended to be the conductive surface that is exposed to the space environment. The bulk resistivities of the CNT layers of the composite films showed a common enhancement of 18 orders of magnitude compared to commercial PI, Kapton HN (25 μm thick), which has a bulk resistivity of 1.5 × 10^{17} Ω cm.[46] The sheet resistivities of the composite films were found to be higher than that of the pure CNT sheet by a factor of 2, an insignificant increase as far as ESD protection is concerned. The fact that the sheet conductivity remained high despite the infiltration of insulating POSS−PI implies that the flow of electrical current was enabled through the entangled CNT network and was not significantly interrupted by the polymer matrix. This observation suggests that the POSS−PI matrix does not penetrate appreciably into the CNT junctions and that the original continuum between adjacent CNTs is largely preserved. In contrast, the insulating polymer does affect the conducivity of CNT junctions in CNT composites that are produced by CNT dispersion.[30]

Table 1. Resistivities of Pure PI (Kapton HN), CNT Sheets, and CNT−POSS−PI Films with POSS Contents of 0, 5, and 15 wt %

sample	average sheet resistivity ±45 (Ω/□)	calculated bulk resistivity (Ω cm)
CNT-15%POSS−PI film	238	0.21
CNT-5%POSS−PI film	219	0.20
CNT−PI film	187	0.17
CNT sheet	95	0.08
Kapton HN[46]		1.5 × 10^{17}

Measuring the resistance for an increasing number of segments also allows for the investigation of the homogeneous morphology along the samples. The linear increase in the lateral resistance with the number of squares, L/w, (Figure 3b) indicates that the CNT sheets were homogeneous after the CVD procedure and that their uniform nature was preserved after the PI and POSS−PI infiltration.

DOI: 10.1021/acsami.5b02200
ACS Appl. Mater. Interfaces 2015, 7, 12047−12056

The mechanism that governs the sheet resistivity was investigated by temperature-dependent measurements. The temperature dependence of the sheet resistivity was measured using the four-point van der Pauw method on 5 mm × 5 mm samples from −160 to 200 °C, in 30 °C intervals. The composite films and pure CNT sheets were tested (one sample of each type), as depicted in Figure 3c, where the data exhibited conduction behavior that corresponds to the three-dimensional (3D) variable range hopping (VRH) conduction mechanism, which is described by

$$\rho_s T^{-1/2} \propto \exp(B/T^{1/4}) \quad (6)$$

where ρ_s is the sheet resistivity, T is the temperature, and B is a constant.[47] The data were plotted as Arrhenius curves of $\ln(\rho_s T^{-1/2})$ versus $T^{-1/4}$ and fit with linear trend lines. The general expression of the resistivity in the VRH model has a temperature dependence of $\exp(B/T^{1/1+d})$, where d is related to the dimensionality of the conductive network. The fact that the data fit the expression $\exp(B/T^{1/4})$ indicates that $d = 3$ and suggests that the electron transport in both CNT sheets and CNT-based composites is consistent with 3D conductivity.[48] Finally, the samples were cooled to 25 °C, and their resistivities increased to their original values with no indication of hysteresis (data not shown). The hopping mechanism is related to the lack of covalent bonding between the stacked cones that characterize the CSCNT structure. Therefore, electrons hop from one defect site to another and between neighboring CNTs. Practically, at room temperature, the electrons possess enough energy to exhibit ohmic conductivity (Figure 3a).

The resistivities of the different samples exhibited a common temperature dependence, as is evident by the similar slopes of the different trend lines. The shift of the different temperature-dependent resistivity plots in the y-axis (Figure 3c) is consistent with the variance in the room-temperature resistivities (Table 1). This result implies an identical conduction mechanism for the different samples, which is determined by an inherent characteristic of the CNT sheet and cannot be related to the PI or POSS content. The fact that the POSS−PI matrix did not influence the resistivity temperature dependence can be attributed not only to the absence of POSS−PI in the CNT junctions but also to the excellent thermal stability of the PI,[49,50] which is apparent from its high glass transition region of 360−410 °C.[46]

3.3. Mechanical Characterization. Tensile tests were performed on the composite films, and stress-versus-strain curves are presented in Figure 4a. The as-grown CNT sheets were not tested due to their brittle nature and lack of mechanical stability. The Young's modulus, UTS, and elongation at break were extracted (Table 2). The CNT−POSS−PI films demonstrated a common Young's modulus (for all POSS contents) of 2.3 GPa, which is close to that of pure commercial PI, Kapton HN (2.5 GPa).[46] The UTS and elongation at break of the CNT−POSS−PI films with 0, 5, and 15 wt % POSS content were found to be lower than that of the pure PI.[46] This result can be related to the original porous nature of the CNT sheet and the absence of polymeric matrix at the CNT junctions. The CNT-based composite's preservation of the original conduction (see section 3.2) further supports this conclusion. Additionally, the UTS decreased as the POSS content increased to 15 wt %, a phenomenon that was reported previously.[18] However, the resulting tensile strengths are still adequate for ESD protection, as thermal blankets are subjected only to minor tensile stresses.

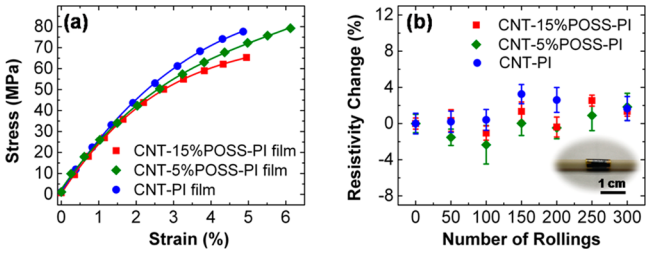

Figure 4. Characterization of CNT−POSS−PI films under mechanical manipulation (0, 5, and 15 wt % POSS content in blue circles, green diamonds, and red squares, respectively). (a) Stress vs strain curves obtained by DMA in tensile test mode. (b) Sheet resistivity change as a function of the number of rolling cycles. (inset) A free-standing composite film rolled around a 2.9 mm diameter rod.

Table 2. Mechanical Properties[a] of Pure PI (Kapton HN), CNT Sheets, and CNT−POSS−PI Films with POSS Contents of 0, 5, and 15 wt %

sample	Young's modulus (GPa)	UTS (MPa)	elongation at break (%)
CNT-15%POSS−PI film	2.3	65	4.9
CNT-5%POSS−PI film	2.3	77	6.1
CNT−PI film	2.3	78	4.9
Kapton HN[46]	2.5	231	72

[a]Young's modulus, UTS, and elongation at break.

The durability of the electrical conductivity of the composite films to bending was examined. Composite films (0.5 cm × 4 cm) were rolled up to 300 times around a ceramic rod of 2.9 mm diameter (Figure 4b, inset). The sheet resistivity of the conductive bottom surface (containing CNTs) was measured after each set of 50 rolling cycles. This flexibility test is considered severe in comparison to similar tests reported in earlier publications due to the small bending diameter.[51] Figure 4b shows the sheet resistivity change versus the number of rolling cycles for one representative CNT−POSS−PI film of each POSS content (0, 5, and 15 wt %). Ten repetitions of each resistivity measurement were performed. The resistivity was found to be stable, with insignificant changes of ca. ±3% after 300 rolling cycles. These are among the smallest resistivity changes under bending reported to date.[25,51] In contrast, commercial conductive coatings, such as ITO, are fragile and typically suffer from severe degradation of their electrical conductance as a result of the fracture of the coatings upon bending.[52]

3.4. Durability in a Space Environment. The potential of the composite films for space applications was examined under simulated space environmental conditions, including thermal cycling, ionizing radiation, and AO. The durability of these polyimide composites is not expected to be affected by solar vacuum ultraviolet (VUV) radiation, as the similar polyimide, Kapton, has been shown to be insensitive to VUV radiation.[53]

The operating temperature of the CNT-based films in space is governed by their thermo-optical characteristics α_s and ε. Hence, the thermo-optical properties of the films, measured with an IR/solar reflectometer, are shown in Table 3. The CNT-based films demonstrated an increase in α_s by a factor of 2 compared to that of pure PI (Kapton). The α_s increase, which

DOI: 10.1021/acsami.5b02200
ACS Appl. Mater. Interfaces 2015, 7, 12047−12056

Table 3. Thermo-Optical Properties of Pure PI (Kapton) and CNT−POSS−PI Films with POSS Contents of 0, 5, and 15 wt %

sample	α_s	ε	α_s/ε	T_{max} (°C)
CNT-15%POSS−PI film	0.99	0.80	1.25	21.6
CNT-5%POSS−PI film	0.99	0.80	1.25	21.6
CNT−PI film	0.99	0.82	1.22	19.8
Kapton[1]	0.48	0.81	0.59	−28.8

is reflected in the black appearance of the CNT-based composites, was caused by the blackbody nature of the CNT-content.[54,55] This phenomenon is well-known from previously studied CNT−PI films for space applications, where an α_s increase by a factor of 5 was reported at a CNT loading of 0.08 wt %.[25] Yet, the impact of the higher α_s on the total thermal blanket's properties is negligible because the CNT-based films are designed only as the outer layer of relatively thick thermal blankets (containing ~20 layers).[2]

According to eq 2, the rise of the CNT-based composites' α_s involves an increase in their operating temperatures in space compared to that of pure PI (Kapton). The maximum temperatures that the CNT-based films are expected to experience in space were calculated using eq 2 and are shown in Table 3, assuming a spherical geometry and a solar flux S of 1366.1 W m^{-2}.[36] The resulting maximum temperatures are compatible with outer-layer thermal blanket applications.

The performance of the CNT−POSS−PI films was investigated under extreme thermal cycling, a common hazard of the space environment. The composite films (5 mm × 5 mm) were subjected to 29 thermal cycles from −100 to 140 °C using a temperature-controlled stage in a nitrogen atmosphere. The sheet resistivities of the CNT−POSS−PI films (5 and 15 wt % POSS content) were measured at the conductive bottom surfaces (containing CNTs) using the four-point van der Pauw method at the minimum and maximum temperatures after every second cycle (Figure 5). The stability of the electrical

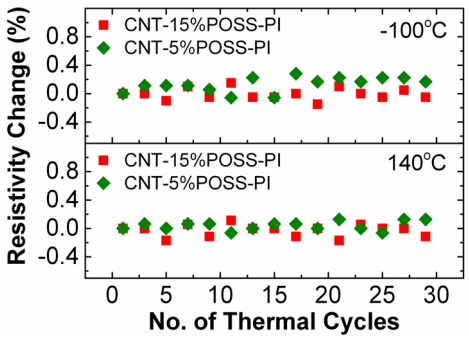

Figure 5. Sheet resistivity change at −100 °C (upper graph) and 140 °C (lower graph) as a function of the number of thermal cycles for CNT−POSS−PI films (5 and 15 wt % POSS content) in green diamonds and red squares, respectively.

conductivity under thermal cycling was demonstrated, indicating compatibility of the CNT−POSS−PI films for space applications, similar to what was reported for a CNT−PI film with 0% POSS content.[29] This test is considered severe due to heating to higher temperature in comparison to the calculated maximum temperatures mentioned above (Table 3).

Another LEO hazard is ionizing radiation, which is dominated by electrons and generally simulated by γ radiation. To explore the films' durability, CNT−PI and CNT-15% POSS−PI films (0.5 cm × 4 cm) were exposed to γ radiation using a ^{60}Co source. The sheet resistivity change of the conductive bottom surface (containing CNTs) was monitored after different γ radiation doses as shown in Table 4. The sheet resistivity of the films changed insignificantly after 9.9 MGy, an equivalent radiation dose to a mission duration of 15 years in GEO or thousands of years in LEO.[41]

Table 4. Sheet Resistivity Change of CNT−PI and CNT-15% POSS−PI Films under γ Irradiation

	resistivity change (%)	
sample	after 7.3 MGy	after 9.9 MGy
CNT-15%POSS−PI	9 ± 4	12 ± 5
CNT−PI	−2 ± 2	0 ± 2

Exposure to AO, the dominant atmospheric species at LEO altitudes, causes erosion of polymeric materials. The CNT−POSS−PI films (0, 5, and 15 wt % POSS content) were exposed to various AO fluences between 6.0 × 10^{19} and 2.9 × 10^{20} O atoms cm^{-2}. During exposure, the films were attached to Si substrates with their conductive bottom surface (containing CNTs) facing up. Nine CNT−POSS−PI films were studied by HRSEM (Figure 6), forming a matrix of varying POSS contents (0, 5, and 15 wt %) and different atomic oxygen fluences (0, 6.0 × 10^{19}, and 2.3 × 10^{20} O atoms cm^{-2}).

Figure 6a−c presents HRSEM images of the bottom surfaces of the unexposed composite films before AO exposure. The homogeneous distribution of the CNTs is evident although the coverage of the polymeric matrix is slightly different from one sample to another. In addition, the unexposed samples appear black in the macroscopic images, as shown in the insets. Exposure of the CNT−PI film's bottom surface to 6.0 × 10^{19} O atoms cm^{-2} caused an erosion of the infiltrated PI matrix, leaving a CNT network exposed to AO attack without a supporting matrix (Figure 6d). The AO-induced damage of the CNT network is clearly seen in the form of truncated CNT tips. Under the same fluence, the HRSEM images of the CNT−POSS−PI films (5 and 15 wt % POSS, Figure 6e,f, respectively) demonstrate a common erosion phenomenology (as opposed to the CNT−PI film), which is characterized by clusters rather than revealed CNTs. The CNT−POSS−PI films showed a similar clustered structure and appeared black in the macroscopic images (insets) after exposure to 2.3 × 10^{20} O atoms cm^{-2} (5 and 15 wt % POSS, Figure 6h,i, respectively). However, the CNT−PI film exposed to the same fluence (2.3 × 10^{20} O atoms cm^{-2}) exhibited a complete erosion of the CNT−PI layer (Figure 6g), revealing the remaining PI layer as seen by the amber appearance of the film in the macroscopic image (inset).

The CNT−PI film eroded under AO exposure because both its components are carbon-based and can form volatile oxides. After exposure to O atoms with a fluence of 6.0 × 10^{19} O atoms cm^{-2}, the PI matrix was eroded first, revealing the CNT network (Figure 6d), most likely as a result of the higher erosion yield of the PI matrix compared to that of the CNTs. This assumption is supported by previous reports of relatively low erosion yield of carbon structures, such as amorphous carbon or highly oriented pyrolytic graphite (HOPG).[1,56,57] After exposure to 2.3 × 10^{20} O atoms cm^{-2}, the CNT−PI film exhibited no apparent CNTs (Figure 6g) as well as a color change (inset). Both observations indicate that the 9 μm thick

DOI: 10.1021/acsami.5b02200
ACS Appl. Mater. Interfaces 2015, 7, 12047−12056

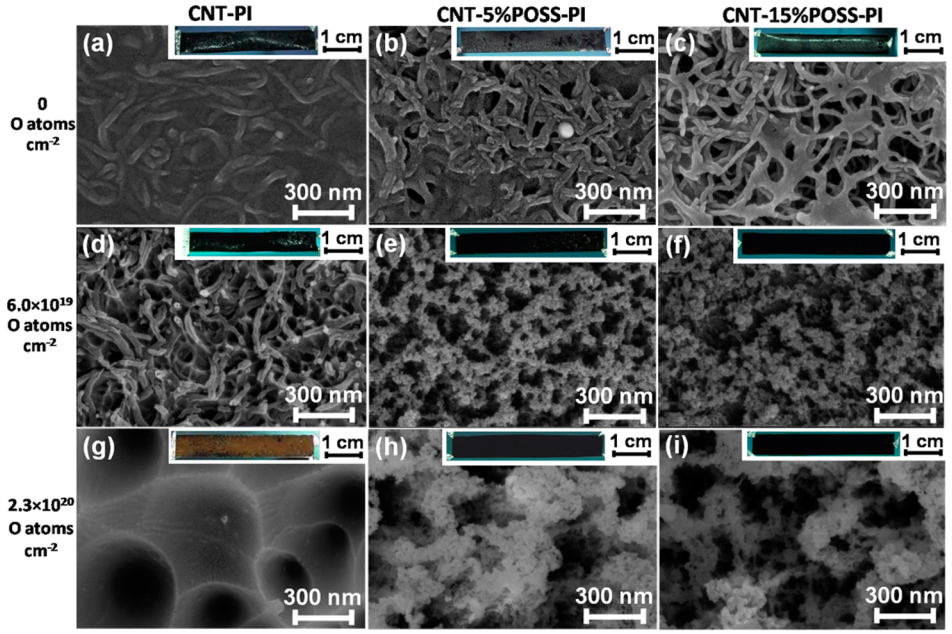

Figure 6. HRSEM images of CNT−POSS−PI films (0, 5, and 15 wt % POSS content) under AO fluences of 0, 6.0×10^{19}, and 2.3×10^{20} O atoms cm^{-2} (macroscopic images as insets).

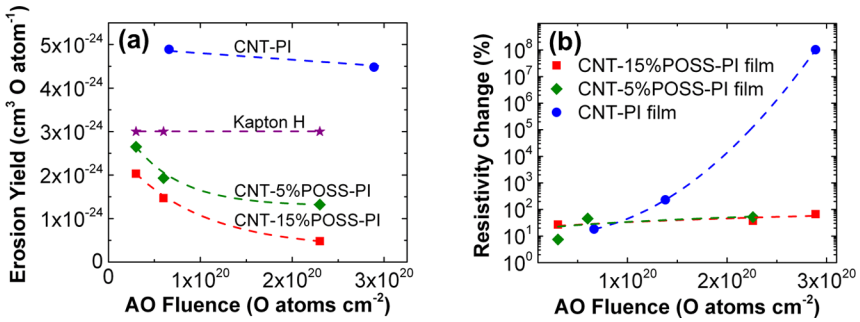

Figure 7. Influence of AO exposure on CNT−POSS−PI films (0, 5, and 15 wt % POSS content) in blue circles, green diamonds, and red squares, respectively. (a) Erosion yields of the composite films and Kapton H (purple stars) as a function of AO fluence. (b) Sheet resistivity changes of the composite films as a function of AO fluence.

CNT−PI layer completely eroded, leaving the excess PI layer that was originally devoid of CNTs.

The CNT−POSS−PI cluster formation resulted from oxidation of the POSS (Si_2O_3) to SiO_2. The SiO_2 layer is stable and inert to AO attack, thus serving as a protective coating for the CNT network. Both 5 and 15 wt % POSS-containing films show an increase in the size of the clusters with increasing AO fluence (Figure 6h,i). This phenomenon indicates a progression in the formation of the O atom-induced passivating layer.

The erosion yields of the CNT−POSS−PI films (0, 5, and 15 wt % POSS content) were determined for varying fluences (Figure 7a) and compared to the accepted erosion yield of Kapton H (3.0×10^{-24} cm^3 O $atom^{-1}$).[1,42] The erosion yields of two CNT−PI films were measured under AO fluences of 6.0×10^{19} and 2.9×10^{20} O atoms cm^{-2}. The resulting values under the different fluences were found to be similar, with an average erosion yield of 4.7×10^{-24} cm^3 O $atom^{-1}$ (156% of the erosion yield of Kapton H). The erosion yields of six CNT−POSS−PI films (three of each POSS content, 5 and 15 wt %) were measured under varying fluences, demonstrating a sharp decrease in the erosion yield with increasing AO fluence and a steady state at higher fluences. The erosion yields of the CNT−POSS−PI films (5 and 15 wt % POSS content) at the maximum AO fluence of 2.3×10^{20} O atoms cm^{-2} were 1.32×10^{-24} and 4.80×10^{-25} cm^3 O $atom^{-1}$, respectively (43% and 16% of the erosion yield of Kapton H). These data were fit well with the empirical equation, $E = Ae^{-F/\tau} + y_0$, with $A = 2.4 \times 10^{-24}$ and 1.7×10^{-24} cm^3 O $atom^{-1}$, $\tau = 5.3 \times 10^{19}$ and 8.6×10^{19} O atoms cm^{-2}, and $y_0 = 1.3 \times 10^{-24}$ and 3.1×10^{-25} cm^3 O $atom^{-1}$ for the CNT−POSS−PI films with 5 and 15 wt % POSS content, respectively. The variables E and F represent erosion yield and fluence, respectively. The parameters A, τ, and y_0 represent the erosion yield at the minimum fluence, the time constant for the decay in the erosion yield, and the erosion yield at infinite fluence, respectively. The decrease and the following stabilization of the erosion rates of the POSS-containing films as a function of O atom fluence are caused by the O atom-induced formation of a passivation layer that ultimately limits the erosion rate, as was previously reported.[16,17]

The etch depth of the CNT-15%POSS−PI film during exposure to 2.3×10^{20} O atoms cm^{-2} (equivalent to ~4 months in 500 km altitude) was evaluated as 1.45 μm from its mass loss according to eq 4. According to the limiting value of the erosion rate, $y_0 = 3.1 \times 10^{-25}$ cm^3 O $atom^{-1}$, the remaining

DOI: 10.1021/acsami.5b02200
ACS Appl. Mater. Interfaces 2015, 7, 12047−12056

7.55 μm will erode completely after an additional fluence of 2.4 $\times$ 10^{21} O atoms cm^{-2} (equivalent to ~4 years at an altitude of 500 km), according to eq 5. Thus, a 9 μm thick CNT layer in a CNT-15%POSS−PI composite film would be expected to remain conductive for a few years in LEO. For longer missions, a thicker CNT layer could be exploited. For example, a 20 μm thick CNT-15%POSS−PI film could be functional for more than 10 years.

In contrast to the CNT−POSS−PI films, the erosion rate of the CNT−PI film is approximately constant with AO fluence, resulting from an unchanged chemical structure of the eroded surface, similar to the pure PI behavior. The higher erosion yield of CNT−PI compared to pure PI may be caused by imperfections in the interface between the CNT sheets and polymeric matrix. Such imperfections can create voids that allow accelerated AO penetration, resulting in a higher erosion yield. The effect of these imperfections was observed also in the degradation of the mechanical properties of the CNT-based composites (see Section 3.3).

The sheet resistivities of nine CNT−POSS−PI films (three of each POSS content, 0, 5, and 15 wt %) were measured along the conductive bottom surface (containing CNTs) after exposure to varying AO fluences, and resistivity change versus the AO fluence is plotted in Figure 7b. The resistivity of the CNT−PI film drastically increased as a result of the exposure. However, the CNT−POSS−PI films (5 and 15 wt % POSS) demonstrated nearly constant resistivity under AO attack. These results are in agreement with the AO erosion mechanisms that were suggested according to the surface morphology modifications displayed in Figure 6. The increase in the resistivity of the CNT−PI films can be related to damage in the continuum of the conductive CNT network that was evidenced by the chopped CNT tips (Figure 6d) and the complete erosion of CNTs (Figure 6g). On the other hand, the electrical conductivity preservation of the 5 and 15 wt % POSS-containing films was due to the coverage of the CNT network coverage by the AO-induced passivation layer (Figure 6e,f,h,i) that protects the conductive CNT network continuum.

4. SUMMARY AND CONCLUSIONS

Electrically conductive and flexible CNT−POSS−PI films for LEO applications were developed by infiltrating POSS−PI blends into CVD-grown entangled CNT sheets. The method employed prevents CNT agglomeration and degradation, which are common in dispersion-based processes. This method is also usable for large film production that is limited only by the size of the CVD reactor. CNT−POSS−PI films with POSS content of 0, 5, and 15 wt %, were investigated. The composite films demonstrated sheet resistivities as low as 200 Ω/□, essentially preserving the original CNT sheet resistivity. Additionally, the low resistivity was found to be stable under bending, which is an advantage over commonly used, and typically fragile, ITO coatings. Moreover, the CNT−POSS−PI films performed well in simulated space environment tests that considered the hazards of thermal cycling, ionizing radiation, and AO. The high electrical conductivity of the CNT−POSS−PI films (5 and 15 wt % POSS content) was preserved after exposure to AO fluences of 2.3 $\times$ 10^{20} O atoms cm^{-2}. Furthermore, CNT-15%POSS−PI films showed a low erosion yield of 4.8 $\times$ 10^{-25} cm^3 O $atom^{-1}$ at this fluence, with an estimated erosion yield of 3.1 $\times$ 10^{-25} cm^3 O $atom^{-1}$ at very high fluences, ~1 order of magnitude lower than that of pure PI. Overall, CNT−POSS−PI composites with 15 wt % POSS content offer a promising route toward utilization of CNTs in space applications, in particular for ESD protection of thermal blankets in the presence of high AO fluxes.

AUTHOR INFORMATION

Corresponding Author

*Phone: +972-8-943-4437. E-mail: nurita@soreq.gov.il.

Notes

The authors declare no competing financial interest.

ACKNOWLEDGMENTS

The authors thank M. David-Pur and D. Rabinovich, for the CVD growth of the CNT sheets, and A. Zentner, M. Ozeri, and S. Glam for experimental assistance. We thank M. Ozeri also for useful discussions. We thank Prof. R. Kalish and Dr. C. Saguy for the use of the van der Pauw sheet resistance measurement system. The atomic-oxygen exposures at Montana State Univ. were supported by the U.S. Air Force Office of Scientific Research: FA9550-10-1-0563. V.J.M is grateful for support awarded by DoD, Air Force Office of Scientific Research, National Defense Science and Engineering Graduate (NDSEG) Fellowship, 32 CFR 168a through the National Defense Science & Engineering Graduate Fellowship Program.

REFERENCES

(1) Tribble, A. C. *The Space Environment;* Princeton University Press: Princetone, NJ, 1995.

(2) Finckenor, M.; Dooling, D. *Multilayer Insulation Material Guidelines,* NASA/TP-1999-209263; National Aeronautics and Spcae Administration: Washington, D.C., 1999.

(3) Ghosh, M.; Mittal, K. *Polyimides: Fundamentals and Applications;* Marcel Dekker: New York, NY, 1996.

(4) Reddy, M. R.; Srinivasamurthy, N.; Agrawal, B. Atomic Oxygen Protective Coatings for Kapton Film: a Review. *Surf. Coat. Technol.* **1993**, *58*, 1−17.

(5) Banks, B. A.; Snyder, A.; Miller, S. K.; De Groh, K. K.; Demko, R. Atomic-Oxygen Undercutting of Protected Polymers in Low Earth Orbit. *J. Spacecr. Rockets* **2004**, *41*, 335−339.

(6) Angirasa, D.; Ayyaswamy, P. S. Review of Evaluation Methodologies for Satellite Exterior Materials in Low Earth Orbit. *J. Spacecr. Rockets* **2014**, *51*, 750−761.

(7) Gotlib-Vainstein, K.; Gouzman, I.; Girshevitz, O.; Bolker, A.; Atar, N.; Grossman, E.; Sukenik, C. N. Liquid Phase Deposition of a Space-Durable, Antistatic, SnO_2 Coating on Kapton. *ACS Appl. Mater. Interfaces* **2015**, *7*, 3539−3546.

(8) Packirisamy, S.; Schwam, D.; Litt, M. Atomic Oxygen Resistant Coatings for Low Earth Orbit Space Structures. *J. Mater. Sci.* **1995**, *30*, 308−320.

(9) Kleiman, J.; Tennyson, R. C. *Protection of Materials and Structures from the Low Earth Orbit Space Environment;* Springer: New York, 1999; Vol. 2.

(10) Iskanderova, Z.; Kleiman, J.; Morison, W.; Tennyson, R. Erosion Resistance and Durability Improvement of Polymers and Composites in Space Environment by Ion Implantation. *Mater. Chem. Phys.* **1998**, *54*, 91−97.

(11) Gudimenko, Y.; Ng, R.; Kleiman, J.; Iskanderova, Z.; Tennyson, R.; Hughes, P.; Milligan, D.; Grigorevski, A.; Shuiski, M.; Kiseleva, L. In *Enhancement of Surface Durability of Space Materials and Structures in LEO Environment;* Proceedings of the 9th International Symposium on Materials in a Space Environment, Noordwijk, The Netherlands, June 16-20, 2003; ESA Publications: Noordwijk, The Netherlands, 2003; pp 95−106.

(12) Wang, M.; Zhao, X.; Shen, Z.; Ma, S.; Xing, Y. Effects of Plerospheres on the Atomic Oxygen Resistance of a Phenolic Resin Composite. *Polym. Degrad. Stab.* **2004**, *86*, 521−528.

DOI: 10.1021/acsami.5b02200
ACS Appl. Mater. Interfaces 2015, 7, 12047−12056

(13) Watson, K. A.; Palmieri, F. L.; Connell, J. W. Space Environmentally Stable Polyimides and Copolyimides Derived from [2, 4-bis (3-aminophenoxy) phenyl] Diphenylphosphine Oxide. *Macromolecules* **2002**, *35*, 4968−4974.
(14) Fischer, H. R.; Tempelaars, K.; Kerpershoek, A.; Dingemans, T.; Iqbal, M.; Lonkhuyzen, H. v.; Iwanowsky, B.; Semprimoschnig, C. Development of Flexible LEO-resistant PI Films for Space Applications using a Self-Healing Mechanism by Surface-Directed Phase Separation of Block Copolymers. *ACS Appl. Mater. Interfaces* **2010**, *2*, 2218−2225.
(15) Miyazaki, E.; Tagawa, M.; Yokota, K.; Yokota, R.; Kimoto, Y.; Ishizawa, J. Investigation into Tolerance of Polysiloxane-Block-Polyimide Film against Atomic Oxygen. *Acta Astronaut.* **2010**, *66*, 922−928.
(16) Brunsvold, A. L.; Minton, T. K.; Gouzman, I.; Grossman, E.; Gonzalez, R. An Investigation of the Resistance of Polyhedral Oligomeric Silsesquioxane Polyimide to Atomic-Oxygen Attack. *High Perform. Polym.* **2004**, *16*, 303−318.
(17) Minton, T. K.; Wright, M. E.; Tomczak, S. J.; Marquez, S. A.; Shen, L.; Brunsvold, A. L.; Cooper, R.; Zhang, J.; Vij, V.; Guenthner, A. J. Atomic Oxygen Effects on POSS Polyimides in Low Earth Orbit. *ACS Appl. Mater. Interfaces* **2012**, *4*, 492−502.
(18) Verker, R.; Grossman, E.; Eliaz, N. Erosion of POSS-Polyimide Films under Hypervelocity Impact and Atomic Oxygen: the Role of Mechanical Properties at Elevated Temperatures. *Acta Mater.* **2009**, *57*, 1112−1119.
(19) Verker, R.; Grossman, E.; Gouzman, I.; Eliaz, N. Residual Stress Effect on Degradation of Polyimide under Simulated Hypervelocity Space Debris and Atomic Oxygen. *Polymer* **2007**, *48*, 19−24.
(20) Verker, R.; Grossman, E.; Gouzman, I.; Eliaz, N. TriSilanol-Phenyl POSS−Polyimide Nanocomposites: Structure−Properties Relationship. *Compos. Sci. Technol.* **2009**, *69*, 2178−2184.
(21) Chou, W.-J.; Wang, C.-C.; Chen, C.-Y. Characteristics of Polyimide-based Nanocomposites Containing Plasma-Modified Multi-Walled Carbon Nanotubes. *Compos. Sci. Technol.* **2008**, *68*, 2208−2213.
(22) Jiang, X.; Bin, Y.; Matsuo, M. Electrical and Mechanical Properties of Polyimide−Carbon Nanotubes Composites Fabricated by in situ Polymerization. *Polymer* **2005**, *46*, 7418−7424.
(23) Ogasawara, T.; Ishida, Y.; Ishikawa, T.; Yokota, R. Characterization of Multi-Walled Carbon Nanotube/Phenylethynyl Terminated Polyimide Composites. *Composites, Part A* **2004**, *35*, 67−74.
(24) Ounaies, Z.; Park, C.; Wise, K.; Siochi, E.; Harrison, J. Electrical Properties of Single Wall Carbon Nanotube Reinforced Polyimide Composites. *Compos. Sci. Technol.* **2003**, *63*, 1637−1646.
(25) Smith, J.; Connell, J.; Delozier, D.; Lillehei, P.; Watson, K.; Lin, Y.; Zhou, B.; Sun, Y. P. Space Durable Polymer/Carbon Nanotube Films for Electrostatic Charge Mitigation. *Polymer* **2004**, *45*, 825−836.
(26) So, H. H.; Cho, J. W.; Sahoo, N. G. Effect of Carbon Nanotubes on Mechanical and Electrical Properties of Polyimide/Carbon Nanotubes Nanocomposites. *Eur. Polym. J.* **2007**, *43*, 3750−3756.
(27) Yuan, W.; Che, J.; Chan-Park, M. B. A Novel Polyimide Dispersing Matrix for Highly Electrically Conductive Solution-Cast Carbon Nanotube-Based Composite. *Chem. Mater.* **2011**, *23*, 4149−4157.
(28) Zhu, B. K.; Xie, S. H.; Xu, Z. K.; Xu, Y. Y. Preparation and Properties of the Polyimide/Multi-Walled Carbon Nanotubes (MWNTs) Nanocomposites. *Compos. Sci. Technol.* **2006**, *66*, 548−554.
(29) Atar, N.; Grossman, E.; Gouzman, I.; Bolker, A.; Hanein, Y. Reinforced Carbon Nanotubes as Electrically Conducting and Flexible Films for Space Applications. *ACS Appl. Mater. Interfaces* **2014**, *6*, 20400−20407.
(30) Ma, P. C.; Siddiqui, N. A.; Marom, G.; Kim, J. K. Dispersion and Functionalization of Carbon Nanotubes for Polymer-Based Nanocomposites: a Review. *Composites, Part A* **2010**, *41*, 1345−1367.
(31) David-Pur, M.; Bareket-Keren, L.; Beit-Yaakov, G.; Raz-Prag, D.; Hanein, Y. All-Carbon-Nanotube Flexible Multi-Electrode Array for Neuronal Recording and Stimulation. *Biomed. Microdevices* **2013**, *16*, 43−53.
(32) TB, Pyralin Polyimide Coating PI 2545 PI 2540, Product Information, Du Pont, February 1993.
(33) Hergenrother, P. M. *Condensation Polyimides,* NASA-TM-103467; NASA Langley Research Center: 1989.
(34) van der Pauw, L. A Method of Measuring Specific Resistivity and Hall Effect of Discs of Arbitrary Shape. *Philips Res. Rep.* **1958**, *12*, 1−9.
(35) Poinas, P. In *The ESA initiative training courses, Small and Medium Sized Enterprises SME04: Satellite Thermal Control Engineering;* 2004.
(36) *Standard Solar Constant and Zero Air Mass Solar Spectral Irradiance Tables,* ASTM E490; ASTM International: West Conshohocken, PA, 2002.
(37) Jung, C.-H.; Kim, D.-K.; Choi, J.-H.; Nho, Y.-C.; Shin, K.; Suh, D.-H. Shortening of Multi-Walled Carbon Nanotubes by γ-Irradiation in the Presence of Hydrogen Peroxide. *Nucl. Instrum. Methods Phys. Res., Sect. B* **2008**, *266*, 3491−3494.
(38) Li, B.; Feng, Y.; Ding, K.; Qian, G.; Zhang, X.; Zhang, J. The Effect of Gamma Ray Irradiation on the Structure of Graphite and Multi-Walled Carbon Nanotubes. *Carbon* **2013**, *60*, 186−192.
(39) Lubkowski, G.; Kuhnhenn, J.; Suhrke, M.; Weinand, U.; Endler, I.; Meibner, F.; Richter, S. Gamma Radiation Effects in Vertically Aligned Carbon Nanotubes. *IEEE Trans. Nucl. Sci.* **2012**, *59*, 792−796.
(40) Nielsen, K. L.; Hill, D. J.; Watson, K. A.; Connell, J. W.; Ikeda, S.; Kudo, H.; Whittaker, A. K. The Radiation Degradation of a Nanotube−Polyimide Nanocomposite. *Polym. Degrad. Stab.* **2008**, *93*, 169−175.
(41) Holmes-Siedle, A.; Adams, L. *Handbook of Radiation Effects;* Oxford University Press: Oxford, U.K., 1993.
(42) Buczala, D. M.; Brunsvold, A. L.; Minton, T. K. Erosion of Kapton H® by Hyperthermal Atomic Oxygen. *J. Spacecr. Rockets* **2006**, *43*, 421−425.
(43) *Standard Practices for Ground Laboratory Atomic Oxygen Interaction Evaluation of Materials for Space Applications,* ASTM E2089−00; ASTM International: West Conshohocken, PA, 2014.
(44) Peplinski, D. R.; Arnold, G. S.; Borson, E. N. In *13th Space Simulation Conf.: Introduction to Simulation of Upper Atmosphere Oxygen Satellite Exposed to Atomic Oxygen in Low Earth Orbit;* NASA: United States, 1984; pp 133−145.
(45) *Packaging Materials for ESD Sensitive Items,* ANSI/ESD S541−2008; ESD Association: United States, 2008.
(46) *Kapton® HN Polyimide Film,* MSDS No. K-15345-1 Technical Data Sheet, Du Pont, April 2011.
(47) Godet, C. Physics of Bandtail Hopping in Disordered Carbons. *Diamond Relat. Mater.* **2003**, *12*, 159−165.
(48) Li, Q.; Li, Y.; Zhang, X.; Chikkannanavar, S. B.; Zhao, Y.; Dangelewicz, A. M.; Zheng, L.; Doorn, S. K.; Jia, Q.; Peterson, D. E. Structure-Dependent Electrical Properties of Carbon Nanotube Fibers. *Adv. Mater.* **2007**, *19*, 3358−3363.
(49) Heltzel, S.; Semprimoschnig, C. O. A Detailed Study on the Thermal Endurance of Kapton HN® and Upilex S®. *High Perform. Polym.* **2004**, *16*, 235−248.
(50) Semprimoschnig, C. O.; Heltzel, S.; Polsak, A.; Van Eesbeek, M. Space Environmental Testing of Thermal Control Foils at Extreme Temperatures. *High Perform. Polym.* **2004**, *16*, 207−220.
(51) Zhu, Y.; Sun, Z.; Yan, Z.; Jin, Z.; Tour, J. M. Rational Design of Hybrid Graphene Films for High-Performance Transparent Electrodes. *ACS Nano* **2011**, *5*, 6472−6479.
(52) Cairns, D. R.; Witte, R. P.; Sparacin, D. K.; Sachsman, S. M.; Paine, D. C.; Crawford, G. P.; Newton, R. Strain-Dependent Electrical Resistance of Tin-Doped Indium Oxide on Polymer Substrates. *Appl. Phys. Lett.* **2000**, *76*, 1425−1427.
(53) Zhang, J.; Lindholm, N. F.; Brunsvold, A. L.; Upadhyaya, H. P.; Minton, T. K.; Tagawa, M. Erosion of FEP Teflon and PMMA by VUV Radiation and Hyperthermal O or Ar Atoms. *ACS Appl. Mater. Interfaces* **2009**, *1*, 653−660.

DOI: 10.1021/acsami.5b02200
ACS Appl. Mater. Interfaces 2015, 7, 12047−12056

(54) Roro, K. T.; Tile, N.; Mwakikunga, B.; Yalisi, B.; Forbes, A. Solar Absorption and Thermal Emission Properties of Multiwall Carbon Nanotube/Nickel Oxide Nanocomposite Thin Films Synthesized by Sol−Gel Process. *Mater. Sci. Eng., B* **2012**, *177*, 581−587.
(55) Camacho, R.; Morgan, A.; Flores, M.; McLeod, T.; Kumsomboone, V.; Mordecai, B.; Bhattacharjea, R.; Tong, W.; Wagner, B.; Flicker, J. Carbon Nanotube Arrays for Photovoltaic Applications. *JOM* **2007**, *59*, 39−42.
(56) Nicholson, K. T.; Minton, T. K.; Sibener, S. Temperature-Dependent Morphological Evolution of HOPG Graphite upon Exposure to Hyperthermal O (^{3}P) Atoms. *Prog. Org. Coat.* **2003**, *47*, 443−447.
(57) Banks, B. A.; de Groh, K. K.; Miller, S. K. *Low Earth Orbital Atomic Oxygen Interactions with Spacecraft Materials,* NASA/TM-2004−213400; National Aeronautics and Spcae Administration: 2004.

DOI: 10.1021/acsami.5b02200
ACS Appl. Mater. Interfaces 2015, 7, 12047−12056